



Cite this: DOI: 10.1039/d4tb00437j

Design-encoded dual shape-morphing and shape-memory in 4D printed polymer parts toward cellularized vascular grafts†

Saswat Choudhury,^a Akshat Joshi,^a Vageesh Singh Baghel,^b G. K. Ananthasuresh,^b Sonal Asthana,^{cd} Shervanthi Homer-Vanniasinkam^{ce} and Kaushik Chatterjee^{id}*^{ac}

Current additive manufacturing technologies wherein as-printed simple two-dimensional (2D) structures morph into complex tissue mimetic three-dimensional (3D) shapes are limited to multi-material hydrogel systems, which necessitates multiple fabrication steps and specific materials. This work utilizes a single shape memory thermoplastic polymer (SMP), PLMC (polylactide-co-trimethylene carbonate), to achieve programmable shape deformation through anisotropic design and infill angles encoded during 3D printing. The shape changes were first computationally predicted through finite element analysis (FEA) simulations and then experimentally validated through quantitative correlation. Rectangular 2D sheets could self-roll into complete hollow tubes of specific diameters (ranging from ≈ 6 mm to ≈ 10 mm) and lengths (as long as 40 mm), as quantitatively predicted from FEA simulations within one minute at relatively lower temperatures (≈ 80 °C). Furthermore, shape memory properties were demonstrated post-shape change to exhibit dual shape morphing at temperatures close to physiological levels. The tubes (retained as the permanent shape) were deformed into flat sheets (temporary shape), seeded with endothelial cells (at $T < T_g$), and thereafter triggered at ≈ 37 °C back into tubes (permanent shape), utilizing the shape memory properties to yield bioresorbable tubes with cellularized lumens for potential use as vascular grafts with improved long-term patency. Additionally, out-of-plane bending and twisting deformation were demonstrated in complex structures by careful control of infill angles that can unprecedentedly expand the scope of cellularized biomimetic 3D shapes. This work demonstrates the potential of the combination of shape morphing and SMP behaviors at physiological temperatures to yield next-generation smart implants with precise control over dimensions for tissue repair and regeneration.

Received 1st March 2024,
Accepted 4th May 2024

DOI: 10.1039/d4tb00437j

rsc.li/materials-b

1. Introduction

Four-dimensional (4D) printing combines three-dimensional (3D) printing of responsive materials with either a specific stimulus and/or smart design, yielding a variety of programmed shape changes over time. It has attracted considerable attention from researchers in the field of additive manufacturing worldwide.¹ It offers unique opportunities to realize complex

structures that are otherwise not possible to manufacture *via* conventional 3D printing or other fabrication technologies. The smart materials used in the printing could either be shape memory polymers (SMPs)² or multi-materials with differential properties in response to a specific stimulus.³ SMPs are characterized by their glass transition temperature (T_g), above which they can be deformed from an original shape into a temporary shape by the application of an external force. They can be fixed in that shape on rapid cooling below T_g by holding the pre-strain and finally be recovered back to the original shape on reheating above T_g to release the pre-strain. This reheating activates the polymer chains, enabling their transition from a glassy state to a rubbery state.⁴ Direct heating is the simplest and most widely explored means of triggering a shape change, as it does not involve any additives or fillers and ensures homogeneous heating in a structure.⁴ Apart from direct heating, SMPs can be doped with appropriate fillers to realize shape change *via* indirect heating, such as inductive heating,⁵ NIR irradiation,⁶ microwave heating,⁷ Joule heating,⁸ focused ultrasound,⁹ *etc.* However, a

^a Department of Bioengineering, Indian Institute of Science, C.V. Raman Avenue, Bangalore, 560012, India. E-mail: kchatterje@iisc.ac.in; Tel: +91-80-22933408

^b Department of Mechanical Engineering, Indian Institute of Science, C.V. Raman Avenue, Bangalore, 560012, India

^c Department of Materials Engineering, Indian Institute of Science, C.V. Raman Avenue, Bangalore, 560012, India

^d Department of Hepatobiliary and Multi-Organ Transplantation Surgery, Aster CMI Hospital, Bangalore, 560024, India

^e Department of Mechanical Engineering and Division of Surgery, University College London, London, UK

† Electronic supplementary information (ESI) available. See DOI: <https://doi.org/10.1039/d4tb00437j>

significant drawback of SMPs is the tedious thermomechanical programming, wherein the intermediate temporary shape is set using external forces, thereby limiting their applications.

There are other strategies that induce pre-strain during the printing process itself, and hence do not rely on the application of an external force post-printing. The strain can either be generated through careful control of the printing parameters,¹⁰ selective placement of heating elements,¹¹ or by encoding anisotropic designs during printing.¹² These techniques can be leveraged for shape morphing immediately post-printing without an additional programming step.

Shape morphing from a pre-programmed shape to a final stable shape is generally less explored in the field of additive manufacturing. The few reported examples are essentially limited to multi-component hydrogels involving gradient crosslinking¹³ or anisotropic design leading to differential swelling rates.¹⁴ However, thermoplastic polymers, including SMPs, have been minimally explored for programming multiple shape deformation. Recent studies have utilized ABS (acrylonitrile butadiene styrene)¹² and PLA (polylactic acid)¹⁵ for filament-based 3D printing and shape change post-printing owing to differential infill patterns and the resultant residual stresses. However, there are severe limitations of ABS such as it exhibits only small shape deformation (for instance, a flat sheet could only deform to an elliptical shape, not a full tube) and at higher temperatures ($\approx 150\text{ }^{\circ}\text{C}$) with a long duration for shape morphing (15 min).¹² Moreover, ABS is non-degradable and not suited for biomedical applications. Similarly, though bio-degradable, PLA is limited by its high T_g ($\approx 70\text{ }^{\circ}\text{C}$) and even higher shape change triggering temperatures ($\approx 150\text{ }^{\circ}\text{C}$),¹⁵ rendering it unsuitable for shape changes in the presence of biomolecules and cells. PLMC (polylactide-co-trimethylene carbonate) is an SMP reported for use as deployable structures in biomedical applications due to its favorable T_g , which is close to physiological temperatures.¹⁶ PLMC is a promising biomaterial for the conversion of 2D shapes to engineered 3D structures under mild conditions, and can be combined with innovative designs to yield smart medical implants. PLMC has been previously combined with inductive-heating responsive iron oxide nanofillers to realize contactless heating under an alternating magnetic field for use as deployable structures.¹⁷ However, a major limitation of such systems is the difficulty in printing the original structures into complex shapes, for relevant biomedical applications.¹⁸ The biological effects of the magnetic particles following degradation of the polymer matrix are poorly understood and need extensive investigations prior to clinical use.

This work aims to address these limitations by developing a versatile platform to employ design-aided additive manufacturing, wherein a single medical-grade SMP is utilized to incorporate anisotropic design encodings during printing to result in predictable and programmable shape changes post-printing. Additionally, the concept of dual shape-morphing was demonstrated in a single SMP, thereby enabling the shape change at much lower temperatures. It should be noted that the retention of shape memory properties post-shape-change has not yet been clearly understood and/or demonstrated. This strategy can

assuage the current drawbacks of the high triggering temperatures of shape change and enable the generation of complex shapes in the presence of cells. In this work, PLMC is utilized for extrusion-based melt-3D printing into design-encoded structures that undergo programmable shape changes at relatively lower temperatures ($\approx 80\text{ }^{\circ}\text{C}$). The shape changes are rapid ($<1\text{ min}$), programmable, and predictable through finite element analysis (FEA) simulations, and yield complete deformation into biomedically relevant shapes, such as complete hollow tubes. The final diameters of the experimentally obtained tubes are in close agreement with the simulation results, achieving a quantitative correlation. These programmable shape changes were then combined with the shape memory attributes of PLMC that can be triggered at even lower temperatures ($\approx 37\text{ }^{\circ}\text{C}$). The utility of the unique attributes of these 4D printed parts capable of dual shape morphing is demonstrated by fabricating cellularized grafts, which have potential benefits in engineering scaffolds for vascular, biliary, and gastrointestinal repair and regeneration.

2. Materials and methods

2.1. 3D printing of PLMC

Medical-grade PLMC (lactide:trimethylene carbonate 70:30) was purchased from Evonik India Pvt Ltd. PLMC in the form of granules was directly used as the raw material for melt-based extrusion 3D printing in BioX (CELLINK). 3D models were designed in SolidWorks, and customized G codes were made by slicing the StereoLithography (.Stl) files generated using Repetier-Host software. The print paths were defined as per the orientation of the strand w.r.t. the print bed. If the extruded strand is parallel to the print bed, it is denoted as L (longitudinal), while it is referred to as T (transverse) if it is orthogonal to the print bed. For homogeneous lamination, four layers of T and L, *i.e.*, TTTT and LLLL were printed to estimate the coefficients of thermal expansion (α) values (as described in Section 2.2). For heterogeneous lamination, an infill pattern of TTLL or (45° , -45°) was chosen, with a uniformly aligned rectilinear pattern and an infill density of 40% to ensure both sufficient material density and negligible overlapping of strands. For each design, at least three samples were printed in the said infill orientation to assess the shape change post-printing. The infill angles were varied in each layer keeping in mind the desired print path and overall structure geometry. These customized G codes were then used to print different structures. Printing parameters were optimized as follows: a nozzle temperature of $200\text{ }^{\circ}\text{C}$, a print speed of 4 mm s^{-1} , a print bed temperature of $25\text{ }^{\circ}\text{C}$, and a printing pressure of 200 kPa . These parameters resulted in reasonably good print resolution and high shape fidelity.

2.2. Material characterization

The thermal properties of PLMC were estimated by DSC (differential scanning calorimetry, TA Instruments Q2000) using a heating rate of $10\text{ }^{\circ}\text{C min}^{-1}$ (ASTM standard). TGA (thermo-gravimetric analysis) was employed to assess the thermal degradation of PLMC using a heating rate of $10\text{ }^{\circ}\text{C min}^{-1}$

(ASTM E1131) under an inert atmosphere. DMA (dynamic mechanical analysis) was employed to estimate the shape recovery properties of PLMC in tension mode using a previous protocol.¹⁹ Briefly, controlled force mode was used with a loading rate of 0.005 MPa min⁻¹ till a maximum stress of 0.025 MPa min⁻¹ and a deformation temperature of 60 °C.

Static tensile properties of the printed rectangular bars (30 × 5 × 1 mm³) in two infill patterns (T and L) were measured using a universal testing machine at a strain rate of 1 mm s⁻¹. To determine the coefficients of thermal expansion (α) of the rectangular bars of two different orientations *i.e.* T and L (printed into original dimensions of 60 × 6 × 1 mm³), they were subjected to hot water post-printing at 80 °C, and the final dimensions (L_f) were recorded using digital calipers. The values were then compared with original dimensions (L_0) in all three directions (x , y , and z) to estimate the strain (ε_i) and α_i by using the following formula.

$$\alpha_i = \frac{\varepsilon_i}{\Delta T} = \frac{1}{\Delta T} \left(\frac{L_f - L_0}{L_0} \right)_i$$

where the subscript i denotes the directions (x , y , z), α_i is the coefficient of thermal expansion in a specified direction, and L_0 and L_f represent the original and final dimensions after thermal treatment with ΔT temperature change, respectively. At least three samples were used for measuring the α values, and mean values are reported.

For the mechanical properties of self-rolled PLMC tubes, DMA was used to perform uniaxial tension at 37 °C with a loading rate of 0.5 N min⁻¹. Cyclic tests were performed at 37 °C under 0.5 N min⁻¹ and a maximum stress of 1 MPa to assess the suitability of PLMC under the pulsatile flow of blood. A creep test was performed at 37 °C under a loading stress of 1 MPa and a loading and recovery time of 1 minute each to estimate the strain recovery performance of PLMC tubes.

2.3. Thermo-triggered shape morphing of PLMC structures

The as-printed PLMC structures were directly exposed to hot water in a beaker at 80 °C. The shape changes were recorded with a high-resolution digital camera. In the case of the flat sheets, the final lengths and diameters were measured using digital calipers. For any given dimension of the flat sheet, at least three such samples were printed, observed for shape changes in hot water, and the lengths and diameters were recorded.

2.4. Constitutive model and FEA simulations

The governing equation and constitutive model to predict the structure deformation and material behavior for this thermo-mechanical phenomenon are shown below:

$$\nabla \cdot \sigma = 0$$

$$\sigma_{ij} = C_{ijkl} \varepsilon_{kl} - C_{ijkl} \alpha_{kl} \Delta T$$

where $\nabla \cdot \sigma = 0$ is the divergence of the second order stress tensor (σ), which, when equated to zero, gives the equilibrium equation of the system, ε_{kl} is the total actual strain in the system, σ_{ij} is the stress caused by mechanical strain and also

Table 1 Estimation of material parameters in T and L infill patterns for FEA simulations

	E (MPa)	ν	α_{11} (°C)	α_{22} (°C)	α_{33} (°C)
L	1.63	0.35	-2.45×10^{-4}	1.15×10^{-4}	2.9×10^{-4}
T	1.33	0.35	1.31×10^{-4}	-1.84×10^{-4}	3.4×10^{-4}

Note: α_{11} , α_{22} and α_{33} are equivalent to α_x , α_y , α_z in the calculation equation shown in Section 2.2. Refer to Table 3 for actual values of the dimensions and calculations of α values.

Table 2 Characteristics of penalties to simulate self-contact during shape deformation

Contact type	Penalty
Normal	0.005
Tangential	0.01

known as thermal stresses, C_{ijkl} is the elasticity tensor, α_{kl} comprises thermal expansion coefficients and ΔT is the temperature difference provided to the system for deformation.

The 3D-printed planar structures are represented as multi-layer single material systems distinguishable only by the encoding directions. The thermal expansion coefficients of the material are different in different directions, making it orthotropic. In our model, the material encoded in longitudinal and transverse directions is considered isotropic for Young's modulus, *i.e.*, $C_{ijkl} = E$ and orthotropic for the coefficient of expansion, *i.e.*, $\alpha_{kl} = \text{diag}(\alpha_{11}, \alpha_{22}, \alpha_{33})$. The values of material properties calculated from experiments for simulations are shown in Table 1.

To predict the shape deformation of the as-printed structures, a computational model was prepared for finite element analysis (FEA) in the commercially available software package Abaqus 2017 (Simulia 2017). 20 node quadratic structured elements (C3D20) were used from the family of 3D stress in standard and explicit models. A static general solver (Full Newton solution technique) was used to produce the steady state deformation of designs by considering the geometric nonlinearity effect. We also considered normal and tangential contact nonlinearity for self-contact into the system of equations with the penalties given in Table 2. The trial-and-error method was used to converge to the following contact penalties to be imposed on all the results shown in the paper.

For the post-processing of simulation results, the location of nodes, which makes an outer circle after the deformation, was probed from the ABAQUS. The location of selected nodes was saved as data points before and after deformation. We used the MATLAB code to best fit the circle in the saved 3D data, wherein the code determines the radius of the tube formed in the simulation. The location of data points was gathered in the middle along the curvature of the tube in each simulation (and radius was measured in experiments likewise) to validate the quantitative equivalence between the two results.

2.5. *In vitro* cell culture

HUVECs (human umbilical vein endothelial cells, Lonza Biosciences) were passaged in an endothelial growth medium (Biogenics Lifecare), supplemented with 1% antibiotic and other

growth factors, as per the manufacturer's protocol. Cells at passages 2–3 were utilized for cell seeding. The as-printed PLMC structures were sterilized by washing them in 70% ethanol and exposed to UV light for 30 min. The sterilized structures were then conditioned in the complete medium for 24 h prior to cell seeding to aid sufficient protein adsorption. For evaluation of cell viability, the Alamar Blue assay was performed by incubating the samples with the reagent, following the manufacturer's protocol (10% (v/v)), using a working concentration of $100 \mu\text{g mL}^{-1}$ resazurin solution prepared in complete medium. Briefly, 3D-printed discs completely occupied the base of the 48 well plates used. Sterilized discs were seeded with endothelial cells at 30 000 cells per disc, and growth was monitored for up to 5 days. At each time point, scaffolds were incubated with the Alamar Blue reagent (10% v/v in complete medium) for 2 h; thereafter, fluorescence was recorded at wavelengths of excitation/emission: 530/560 nm using a microplate reader (Biotek).

To monitor the cell coverage, morphology, and formation of the endothelial lining, the as-printed pre-programmed flat sheets were first rolled into tubular constructs. The tubular constructs (permanent shape) were deformed back into flat sheets (temporary shape) for efficient seeding (seeding density of 1×10^5 cells per flat sheet at RT) in 6 well plates and were left undisturbed for 1 h to allow cellular attachment. Since the temperature was maintained at room temperature ($\approx 25^\circ\text{C}$), the flat sheets retained their shape. Subsequently, the plates were transferred to a CO_2 incubator at 37°C to allow shape deformation into hollow tubes (permanent shape), and cells were allowed to grow for 5 days. At different time points, live/dead staining (2 μM Calcein AM and 4 μM ethidium homodimer, ThermoFisher Scientific) was performed to visualize the fraction of viable cells. The morphology of the seeded cells was analyzed on days 3 and 5 using an epifluorescence microscope (IX-53, Olympus) after fixing the constructs with 3.7% paraformaldehyde, permeabilizing with 0.1% Triton-X, and staining them with 20 nM Phalloidin (Alexa fluor 488, ThermoFisher Scientific) and $2 \mu\text{g mL}^{-1}$ Hoechst (Thermo Fisher Scientific). Images were captured after flattening the tubes to allow easy visualization of cell coverage over time. Additionally, stained tubular scaffolds were also observed in cross-section to visualize the developed endothelium lining.

2.6. Statistical analysis

The results are presented as mean \pm standard error for each group. GraphPad Prism 5.04 was used for the statistical analysis (GraphPad Software, San Diego, CA, USA). One-way ANOVA was used for the statistical analysis, which was then followed by Dunnett and Tukey tests for significance. All analyses were carried out at a 95% confidence level and were significant at statistical probability (p -value) < 0.05 . Statistical significances were denoted as (*), (**), and (***) for $p < 0.05$, $p < 0.01$, and $p < 0.001$, respectively.

3. Results

Among several types of SMPs, including solvent-responsive,²⁰ photo-responsive,²¹ *etc.*, thermo-triggered SMPs present unique

advantages of exhibiting uniform shape recoveries and higher shape recovery ratios. In this study, a medical-grade thermal triggered PLMC was used owing to its favorable T_g , which is close to physiological temperatures and would be well-suited for exhibiting shape changes in the presence of cells. Melt-extrusion 3D printing was employed to fabricate PLMC into different structures. Melt-extrusion-based printing offers some benefits over other printing modalities, such as direct-ink writing, the absence of toxic solvents and well-controlled and reproducible generation of residual thermal stresses, which leads to programmable shape changes.²²

3.1. Thermal and thermo-mechanical characterization

The thermal and thermomechanical properties of PLMC were characterized, including its T_g , thermal degradation profile, and shape memory performance using DSC (differential scanning calorimetry), TGA (thermogravimetric analysis), and DMA (dynamic mechanical analysis), respectively (all data are compiled in Fig. S1, ESI†). The second heating curve in DSC reveals the glass transition (T_g), cold crystallization (T_{cc}), and melting phenomena (T_m) of PLMC. T_g was estimated at $\approx 37^\circ\text{C}$, T_{cc} at 113°C and T_m at 154°C . It is reported that T_g of a copolymer depends on the monomer ratio, molecular weight, crystallinity, *etc.*²³ Specifically, for PLMC used in this study with a LA:TMC ratio of 70:30, the $T_g \approx 37^\circ\text{C}$ from DSC corroborates with those reported in similar studies.²⁴ On the other hand, TGA reveals a single-step degradation and the onset of thermal degradation is at $\approx 275^\circ\text{C}$. Using the melting and thermal degradation temperatures, the printing temperature was optimized at $\approx 200^\circ\text{C}$, ensuring that the polymer is sufficiently shear thinned in the molten state and is thermally stable without degrading. DMA, which measures the T_g by capturing the mechanical vibrations in polymeric chains, reveals the T_g to be $\approx 50^\circ\text{C}$. The T_g measured by DSC is different and lower (by 13°C) compared to that measured by DMA because of the different mechanisms used by the two methods for measuring T_g . DSC is sensitive to heat capacity (C_p) changes associated with glass transition, whereas DMA captures the mechanical relaxation phenomenon.²⁵ The shape memory properties of PLMC were excellent, with a shape fixity of $\approx 97\%$ and a shape recovery of $\approx 99\%$ in the first cycle. For cyclic thermomechanical testing, shape fixity and shape recovery were $\approx 92\%$ and $\approx 74\%$ in the first cycle, $\approx 93\%$ and $\approx 82\%$ in the second, and $\approx 93\%$ and $\approx 83\%$ in the third cycle, respectively. This can be attributed to the relatively weak interactions in SMPs that involve only physical crosslinking as net points, which leads to a considerable reduction of recovery ratios in the first cycle, after which it becomes constant in the subsequent cycles.²⁶ These observations are in good agreement with previous studies of cyclic thermomechanical testing of PLMC-based systems.²⁷

3.2. 3D printing of PLMC

Though a few studies reported 3D printing of PLMC for porous bioactive scaffolds¹⁹ and its composites for bone scaffolds²⁸ and liquid sensors,²⁹ it remains a challenge to fabricate these materials into complex architectures, such as a thin-walled

hollow tube. Utilizing the intrinsic shape memory properties of PLMC³⁰ and its composites is insufficient to yield hollow tubes, especially the ones with smaller diameters and larger lengths. In this study, anisotropic design principles were utilized during printing to program the extent and direction of shape deformation post-printing. PLMC was first 3D printed into two specific designs of rectangular bars (dimensions: $60 \times 6 \times 0.4 \text{ mm}^3$) with homogeneous stacking patterns, one longitudinal (L), *i.e.*, parallel to the printing/print bed direction, and the other transverse (T), *i.e.*, orthogonal to the printing direction. The printing direction here refers to the longer axis (along the 60 mm length direction). The printing parameters were optimized based on our previous work¹⁷ and similar work on 3D-printed PLMC and related polymers.³¹ Briefly, the printing temperature is kept at $\approx 50 \text{ }^\circ\text{C}$ higher than the melting point, such that it is also well below the onset of thermal degradation. The as-printed bars were then placed in hot water at $\approx 80 \text{ }^\circ\text{C}$. It was noted that the bar with L infill stacking exhibited shrinkage along its longer axis while it expanded along the width direction. The opposite trend was observed in the T-infill design, as shown in Fig. 1. Accordingly, the coefficients of thermal expansion (α) were calculated to be widely different in all three directions in both the designs (L and T), as compiled in Table 3. These observations can be ascribed to the residual stress generated during printing in a given direction and subsequent recovery of these stresses upon heating to a temperature ($\approx 80 \text{ }^\circ\text{C}$) much higher than T_g . The residual stresses tend to relax in a manner that results in an anisotropic dimensional change in the structure, *i.e.*, a decrease in the printing direction and an increase in the other direction. Moreover, the elastic modulus (E) of PLMC printed in L design was higher than that of T (Fig. S2, ESI[†]), which demonstrates the influence of the infill angle on mechanical properties. It was observed that the L exhibits a higher Young's modulus (1.63 MPa) as well as strain at failure ($\approx 30\%$) than the T infill pattern (1.33 MPa and $\approx 25\%$).

3.3. FEA simulations and design-aided 4D printing of PLMC

Design of 4D printable flat sheets has been a challenging problem due to the following complexities being required to be incorporated while modeling the physics behind the phenomenon.

(a) It is known that when the deformation is large, consideration of geometrical nonlinearity is essential for modeling.^{32,33}

Table 3 Comparison of shape deformation in the as-printed T and L infill stacking at $80 \text{ }^\circ\text{C}$ and the estimated thermal expansion coefficients (α_i)

Infill type	Direction	L_0 (mm)	L_i (mm)	ε_i	α_i ($\times 10^{-4}/^\circ\text{C}$)
Transverse (T)	Length (x)	60.2	60.63	0.43	1.31
	Width (y)	5.9	5.84	-0.06	-1.84
	Height (z)	0.4	0.393	0.007	3.4
Longitudinal (L)	Length (x)	61.3	60.47	-0.83	-2.45
	Width (y)	6.5	6.46	0.04	1.15
	Height (z)	0.4	0.394	0.006	2.9

(b) Contact nonlinearity is also crucial to precisely predict the final shape of the sheet.³⁴

(c) Anisotropic material expansion of the material (PLMC in this case) in three principal directions warrants an orthotropic material model for the thermal expansion coefficient while Young's modulus remains isotropic.¹²

(d) Flat sheets are often made up of two layers with different encoding (or infill) directions, while modeling requires an appropriate material orientation to consider due to the orthotropic behavior of thermal expansion.³⁵

The differential expansion of a bilayer system with different coefficients of thermal expansions in the presence of heat causes out-of-plane deformation. It was found that encoding in longitudinal and transverse directions has different coefficients of thermal expansion and, when laid on top of each other, makes a bilayer system with differential expansion. This generates thermal stresses in the system and, in turn, deformation.

Table 4 shows the diameters of tubes formed due to material encoding at the top (longitudinal) and bottom (transverse) layers that are always at 90° relative to each other. In other design iterations, the bottom layer was kept in a transverse position, and the encoding direction of the top layer was relatively varied from 0° to 180° . It is known that encoding direction θ and $(180^\circ + \theta)$ are the same directions, so the deformation of any direction $(180^\circ + \theta)$ will be identical to the deformation recorded when the encoding direction is θ . When the top layer is at 0° angle, as shown in the middle of Fig. S3 (ESI[†]) (in grey), which is the longitudinal direction, then the relative angle difference between the top and bottom layers is 90° , and that makes the tube as shown in Fig. S3 (ESI[†]). When the angle of the top layer is increased from 0° in the interval of 10° , then the following deformation spectrum was obtained, as shown in Fig. S3 (ESI[†]) for the flat sheet of dimension

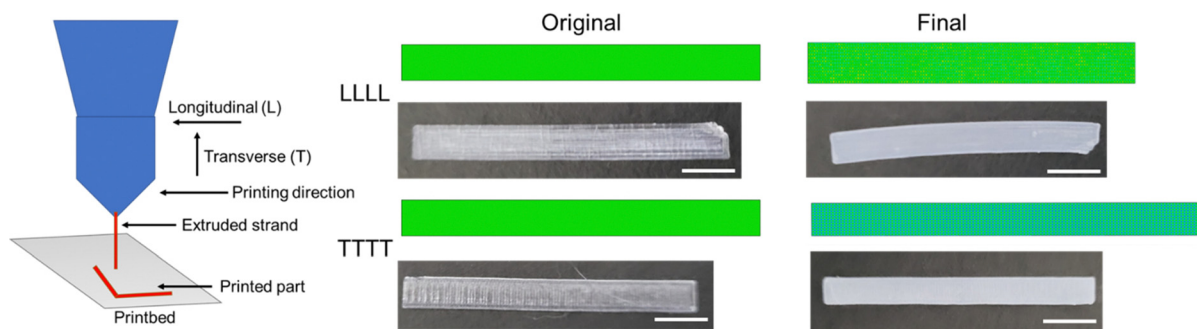


Fig. 1 Thermal deformation of the as-printed PLMC rectangular bars in two infill stackings, as confirmed through FEA simulations and experimental measurements (scale: 10 mm).

Table 4 Quantitative correlation of diameters of hollow tubes obtained from flat sheets between the FEA simulations and the experimental measurements

Original dimensions of flat sheets (in mm ²)	Outer diameters of tubes formed at 80 °C (simulated) (mm)	Outer diameters of tubes formed at 80 °C (experimental) (average ± S.D.) ^a (mm)	Error (in %)
30 × 12	7.02	7.15 ± 0.06	1.85
40 × 12	9.72	9.90 ± 0.02	1.85
25 × 25	6.12	6.25 ± 0.05	2.12
30 × 30	6.35	6.5 ± 0.04	2.36

^a Data are shown for $n = 3$.

30 × 12 × 0.7 (all dimensions in mm). It was observed that the extent of deformation was lesser than the previous angle when the encoding angle was increased on the top layer from 0° to 90°, and the final shapes were also far from the tube shape. As the angle became closer to 90°, no visible deformation occurred, and the sheet remained flat. This trend arises because when the top layer is at 90°, both the top and bottom layers are encoded at the same angle, and there will be no change in the properties between the two layers to experience the out-of-plane deformation. It was also observed that the deformation of flat sheets is mirror symmetric around angle 90°, which implies that the deformation of angles (90° - θ) and (90° + θ) is quantitatively the same, but the direction of deformation is reversed.

The α values, together with E for both L and T infill patterns, were fed into the FEA framework as the material parameters to predict the shape deformation, as shown in Fig. 1 (detailed parameters are compiled in Table 3). Since the extent of deformation was limited in homogeneous stacking, heterogeneous lamination was explored for printed PLMC parts. TTLL (0° infill angle stacked upon the 90° infill angle) design configuration was used to stack two layers of longitudinal patterns over two layers of transverse patterns to induce differential residual stresses during the printing process. In this case, a flat sheet (TTLL) was able to self-roll into a complete hollow tube experimentally when the printed part was exposed to hot water (≈ 80 °C). The same observation was also confirmed from FEA simulations. This phenomenon arises from the significant residual stresses generated in printing combined with different α values for the bottom (T) and top (L) layers and subsequent recovery of the stresses in hot water.

To investigate the influence of infill angles, a variety of angles (0°–180°) were chosen on the top layer while the bottom layer was constant at 90° for simulations. It was seen that maximum bending was obtained when the top layer consisted of infill angles at 0° due to the largest strain generation at the interface in this case (Fig. S3, ESI†). Next, to substantiate the simulation results, a quantitative model was attempted wherein the final diameters of the tubes could be predicted first using different dimensions of the original flat sheets. As seen in Fig. 2, a variety of flat sheets were selected as original shapes in TTLL design and simulated. Next, the same dimensions were used to print flat sheets and then exposed to hot water (at 80 °C) to obtain complete hollow tubes (Fig. 2 and Videos V1, V2, ESI†). A robust quantitative correlation was established between the simulated results and experimental

observations, as seen in Table 4 (difference < 0.2 mm). Hollow tubes with a range of diameters from ≈ 6 mm to ≈ 10 mm can be obtained from flat rectangles and squares. It should be noted that it is extremely challenging to manufacture long hollow tubes by conventional 3D printing, especially ones with diameters less than 8 mm.³⁶ The tubes tend to warp and taper with increasing length. A few earlier studies on the 4D printing of plastics¹² and gels³⁷ either failed to generate complete tubes or lacked precise control over the final diameters of tubes.³⁷ Moreover, the tubes prepared from hydrogels are often soft and not mechanically robust to fulfill the stringent requirements of implantable grafts. As far as thermoplastics are concerned, previous studies on PLA have only achieved partial bending, leading to curved shapes and not complete tubes.^{10,38} In this study, highly stable tubular structures could be prepared with a wide range of diameters and lengths in a predictive and programmable manner. This strategy can minimize the printing time while enabling patient-specific tubular designs through a careful choice of the original dimensions of the flat sheet.

3.4. *In vitro* demonstration of cellularized vascular grafts

Manufacturing vascular grafts of clinically relevant dimensions remains a key biofabrication challenge in the biomedical field, as it demands small diameters and relatively larger lengths.³⁹ Electrospun bilayers,⁴⁰ molded polymer tubes,⁴¹ and 4D printed hydrogels^{42–45} present significant limitations as vascular grafts due to incomplete and unstable shape deformation, complex chemical reactions and short-term patency, and poor mechanical strength, respectively. These limitations are further accentuated if the tubes need to be pre-seeded with cells prior to implantation, as none of the conventional processing techniques can realize cell-laden tubes with high shape fidelity and stability. It is known that small-diameter artificial vascular grafts suffer from acute thrombosis, thickening of the neointimal wall, called intimal hyperplasia, and calcification.⁴⁶ The important challenges that remain unsolved are facilitating rapid re-endothelialization of the luminal surface of the stents and mimicking the complex viscoelastic behavior of the arteries. It is difficult to achieve complete endothelial cell (EC) coverage on stents as the majority of the luminal surface is not in contact with the EC during seeding.⁴⁷ This study attempts to address these plaguing issues by combining the programmable shape deformation with the intrinsic shape memory property of PLMC. It should be noted that all previously reported works on 4D printing of polymers, especially thermoplastics,

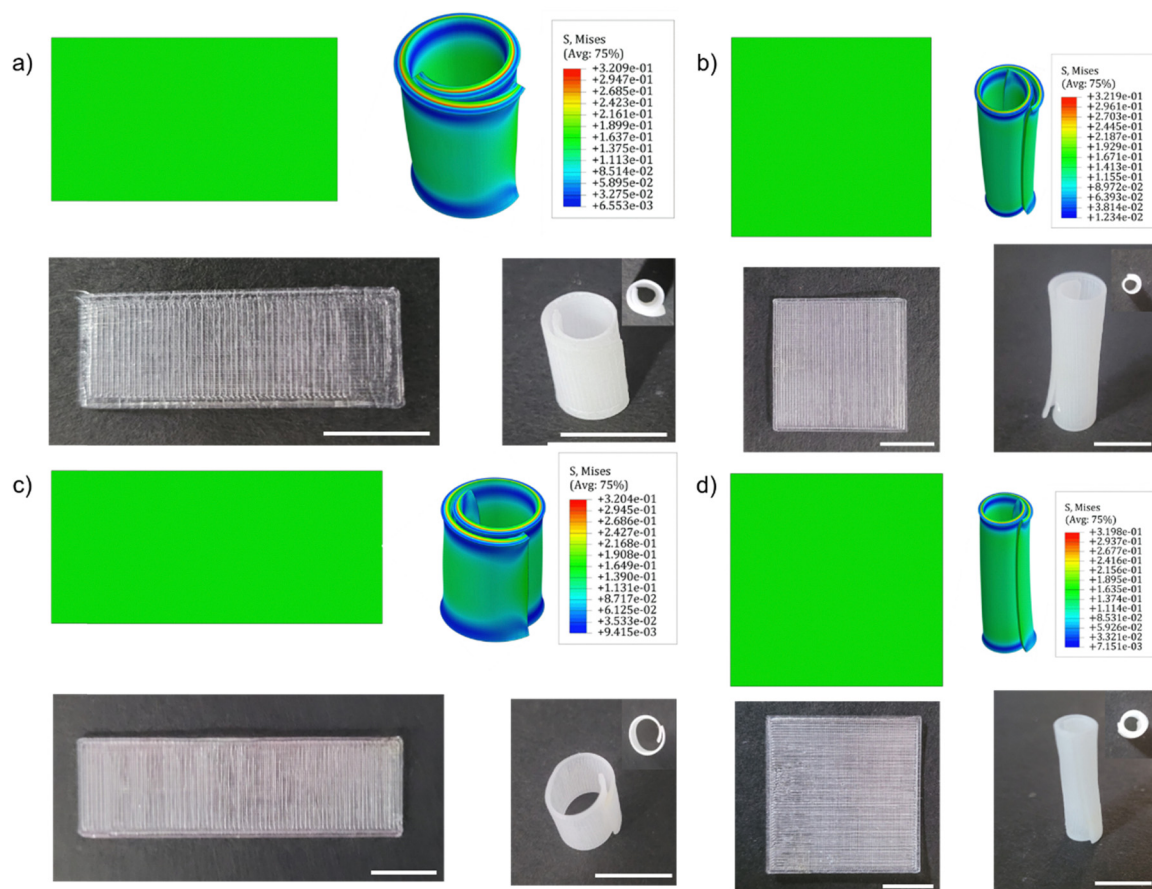


Fig. 2 Quantitative prediction of shape deformation of flat sheets into complete hollow tubes. FEA simulations and the corresponding experimental observations of flat sheets of dimensions (a) $30 \times 12 \text{ mm}^2$, (b) $25 \times 25 \text{ mm}^2$, (c) $40 \times 12 \text{ mm}$, and (d) $30 \times 30 \text{ mm}^2$ into hollow tubes of diameters that are in close agreement (scale: 10 mm).

demonstrate only one-way actuation from an as-printed shape to a final stable shape, wherein the obtained shape is locked.⁴⁸ Given the high temperatures associated with triggering the shape change, one-way actuation is highly restricted in terms of biomedical applications and certainly not feasible in the presence of cells. This necessitates a paradigm shift in the materials and technologies to realize sequential shape-shifting and at physiological levels. In this study, the tubular constructs obtained through direct 4D printing of design-encoded flat sheets act as the stable (permanent) shape. These tubular constructs can be deformed back into planar structures (temporary shape) to re-attain the tubular shape upon reheating $\approx 37 \text{ }^\circ\text{C}$. The second shape change trigger is possible due to the intrinsic shape memory property of PLMC, which is still retained after the pre-programming during the printing process.

First, the response of HUVECs (human umbilical vein endothelial cells) to PLMC was studied by seeding them on printed PLMC structures, as shown in a schematic in Fig. 3a. As seen from the Alamar blue assay results in Fig. 3e, HUVECs were metabolically active and continued to proliferate over time. The adsorption of serum proteins to the cytocompatible polymer facilitated cell adhesion and proliferation.

Next, the feasibility of fabricating cellularized lumens was explored. Briefly, the as-printed design encoded flat sheet was self-rolled into hollow tubes, using design principles that became the stable (permanent) shape for the 3D-printed PLMC part. Next, the tube was deformed back into a flat sheet (temporary shape) at $\approx 40 \text{ }^\circ\text{C}$ ($> T_g$) and fixed by cooling it to $\approx 0 \text{ }^\circ\text{C}$ ($< T_g$). At this stage, HUVECs were seeded on the flat sheet (at room temperature) and allowed to adhere. The samples were left in the hood at room temperature ($\approx 25 \text{ }^\circ\text{C}$) to allow for initial adherence of cells. Thereafter, the sheets were placed inside an incubator operated at $\approx 37 \text{ }^\circ\text{C}$ ($> T_g$) to allow them to self-roll back into the tube of the same dimensions (the permanent shape) owing to its shape memory properties. As seen in Fig. 3(b and c), the tubes that were flattened for imaging revealed well-spread adherent cells with full coverage of the surface by day 5. Low-magnification images (Fig. S4, ESI[†]) also suggest complete cell coverage of the inner surface. The cross-section of the tubes could also be seen laden with HUVECs, as observed in Fig. 3(d). Due to the imaging difficulties given the opaque nature of the PLMC tubes, the cross-sectional view is a representative image of the cellularized tube. The well-defined morphology and tightly formed layer of HUVECs are believed to improve the patency of these grafts

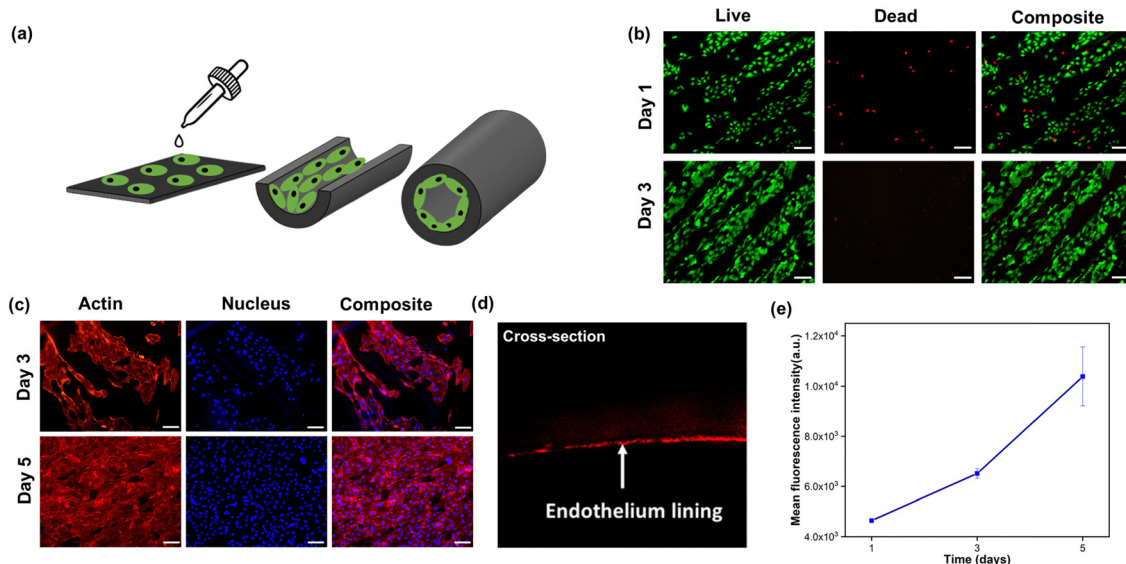


Fig. 3 Dual shape morphing and shape recovery into cellularized hollow tubes for vascular grafts. (a) Schematic of HUVEC-seeded flat sheet morphing into cellularized hollow tubes; (b) live–dead staining showing high viability of HUVECs; (c) actin–nuclear staining highlighting high coverage of HUVECs forming monolayers at day 5; (d) cross-section of hollow tubes showing full confluency of HUVECs; and (e) alamar blue assay showing cell proliferating over time (scale: 100 μm).

when implanted. This unique biofabrication strategy proposed in this work allows for the creation of highly customized vascular tubes of desired dimensions with cell-laden lumens. The advantages of the technique include its amenability to medical grade polymers, the absence of vigorous chemical reactions, and stimulation by cell-friendly temperature changes. This technology can be extended to other kinds of cellularized grafts, such as ureteric and bile duct grafts for placement in ureteric⁴⁹ and biliary reconstruction surgeries,⁵⁰ respectively.

Next, the mechanical properties of printed PLMC structures were assessed to determine their suitability as vascular grafts. The tensile modulus of the PLMC bars ($30 \times 5 \times 1 \text{ mm}^3$) was calculated to be $\approx 8.8 \text{ MPa}$ at 37°C (Fig. S5, ESI[†]), which is comparable to the mechanical properties of native blood vessels, that are in the range of $\approx 11 \text{ MPa}$.⁵¹ This is in good agreement with other reported polymers.¹⁶ Further tuning of the mechanical properties for suiting specific blood vessels can be made by changing the monomer ratio of PLMC or by blending with specific polymers, such as PLGA (poly(lactide-co-glycolide)). Cyclic stress–strain characteristics of PLMC were also investigated to assess the mechanical behavior of the material under repetitive loading and unloading conditions. The results (Fig. S5, ESI[†]) indicate that after some hysteresis during the first cycle, the final strain at the end of each cycle was very close to that of the preceding cycle. Creep results suggest good anti-fatigue properties of PLMC (strain recovery increasing consistently with each cycle and $> 90\%$ by the end of 10 cycles), which can help resist plastic deformation. The irreversible nature of deformation allows the hollow tubes (permanent shape) to maintain their shape. Taken together, the mechanical properties of PLMC indicate that it can well maintain its patency under dynamic loading conditions. However, more detailed studies, especially mechanical behavior

under the pulsatile flow of blood, are needed to further establish the true potential of the self-rolled PLMC tubes as vascular grafts.⁵²

3.5. 4D printing of PLMC into programmable and complex shapes

Furthermore, a variety of planar structures with different infill angles were also explored for programmable shape-changing functionality. In addition to the TTLL design, another infill angle of 45° was chosen to explore multiple shape deformation in a single structure. FEA simulations were used to first predict the final geometries of the as-printed structures. As observed from Fig. 4, a butterfly structure and a cross-shaped structure were simulated first with TTLL and (45° , -45°) designs and then experimentally verified. The butterfly, as well as the cross-shape, curled towards the center in the case of TTLL, and they twisted at the edges in (45° , -45°) as predicted from simulations and corroborated experimentally (Videos V3–V6, ESI[†]). Finally, a flytrap design was also simulated with TTLL design and later printed, and it bent towards the center in both cases at 80°C (Video V7, ESI[†]). This programmable shape deformation can help to realize complex geometries capable of undergoing multiple and predictive shape changes. The designs presented here offer opportunities in soft robotics⁵³ and smart grippers⁵⁴ apart from implantable biomedical devices. Additionally, the effect of dual shape morphing and recovery was demonstrated (Fig. S6, ESI[†]). Briefly, in the first stage, the as-printed shapes morphed spontaneously under the thermal trigger (80°C) into the programmed shapes (new original/permanent shapes). The obtained shapes were then deformed into planar structures (temporary shapes) at $\approx 40^\circ \text{C}$ and fixed by cooling to $\approx 0^\circ \text{C}$ after which the flat shapes could recover back to the programmed shapes (original) at $\approx 37^\circ \text{C}$ due to the

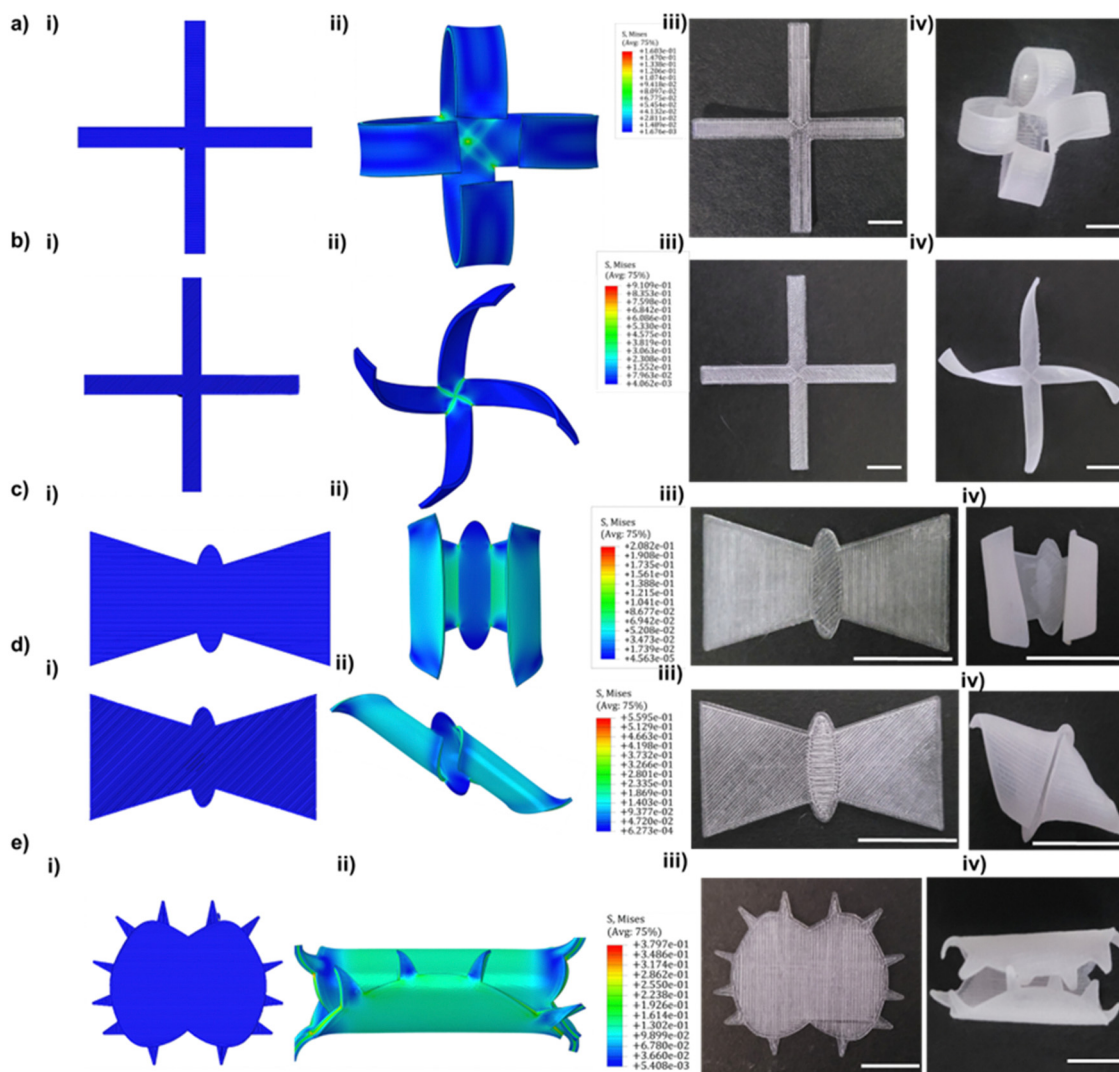


Fig. 4 Programmable shape changes in the as-printed PLMC structures by varying infill angles, as predicted from FEA simulations and confirmed experimentally. (a) Bending and (b) twisting deformation process of a cross shape; (c) bending and twisting deformation of a butterfly shape; (e) bending process of a Venus flytrap. (i) and (ii) Original and simulated final shapes for various geometries with design-encoded infill angles. (iii) and (iv) As-printed shapes with either TLL or $(45^\circ, -45^\circ)$ design encoding and final shapes experiencing bending or twisting movements, respectively, after subjecting to 80°C (scale: 10 mm).

intrinsic properties of the polymer to memorize the shapes. This phenomenon was demonstrated for butterfly and cross shapes printed into TLL and $(45^\circ, -45^\circ)$ design encodings. This concept of triggering the final shape change in such complex shapes at physiological temperatures can be leveraged for use in soft robotics.⁵⁵

Next, more complex shape deformations were realized in a flat sheet by a careful choice of infill angles along the same plane, as seen in Fig. 5. The flat sheet was divided into two parts, one of which had the TLL design encoded and the other encoded with $(45^\circ, -45^\circ)$ infill patterns. This as-printed sheet exhibited simultaneous and complex shape deformation, wherein one half of the sheet (with TLL design) exhibited curling towards the center, while the other half (with $(45^\circ, -45^\circ)$ design) exhibited twisting across its edge, resulting in a final structure (Video V8, ESI†). These exquisite shape changes

can yield bifurcating tubes, which are otherwise extremely challenging to fabricate by conventional techniques. Bifurcated and/or branched tubes are much desired in the form of vascular grafts over simple hollow tubes, especially in the repair and regeneration of complex blood vessel shapes.⁵⁶

4. Discussion

Although as much as 4D printing of polymers has matured in terms of expansion of material candidates, ease of manufacturing, *etc.*, generating hollow tubes of smaller diameters and longer lengths out of thermoplastics with good printing accuracy has always been a challenge. Some studies have modified polymers chemically with supramolecular interactions⁵ or *via* hydrogen bonding,⁵⁷ blending, and addition of reinforcing

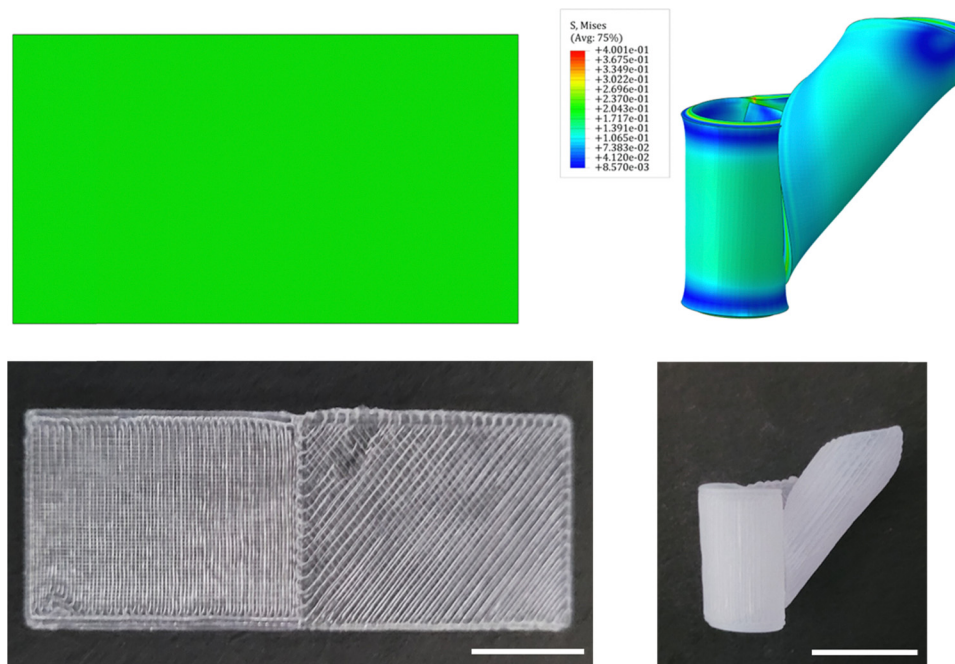


Fig. 5 Simultaneous curling and twisting deformation in the as-printed PLMC flat sheet by two different infill angles in the same plane, as predicted from FEA simulations and confirmed experimentally (scale: 10 mm).

nanomaterials⁵⁸ or small molecule plasticizers to improve their printability. However, it should be noted that these techniques are not universal and are only limited to specific classes of polymers and did not demonstrate the fabrication of any complex structure for relevant biomedical applications. On the other hand, there have been a few studies that investigate biocompatible SMPs with triggering temperatures close to the physiological range for deployable structures, such as PLMC,⁵⁹ PLMC/PTMC (poly(trimethylene carbonate)) with iron oxide nanofillers with inductive-heating responsiveness,⁶⁰ and polyethylene glycol (PEG)/PLA blends as bioinspired intestinal stents,⁶¹ and they have all been explored for the intrinsic shape memory properties of polymers and their composites. It will be difficult to achieve complex shape changes, for instance, out-of-plane bending or twisting, in these cases. This, in turn, severely limits the potential applications that can be expanded by design-aided 3D printing. Table 5 summarizes the recent reports on 4D printing of thermoplastics. Most studies investigate the intrinsic shape memory properties of the SMPs and their composites under direct or indirect heating. This strategy limits the fabrication of complex shapes, such as hollow slender tubes or twisted architectures, and also needs the additional thermomechanical programming post-printing. Moreover, SMP composites are often associated with difficulties in processing,⁶² nanofiller-induced toxicities,⁶³ and needs bulky experimentation in the case of inductive heating. These challenges can be assuaged by inducing strain in the material during the printing process. A few studies report programmable shape changes using ABS and PLA based systems. However, they still need high actuation temperatures to be suitable for biofabrication and fail to achieve

shapes relevant to biomedical applications. This study utilizes anisotropic design principles and a single SMP of medical grade to realize hollow tubes of a range of lengths and diameters accurately and quantitatively predicted from FEA simulations. Additionally, the shape memory property is leveraged to realize sequential shape morphing, resulting in cellularized tubes. The advantage of dual shape morphing lies in the fact that the first step of the shape change allows the self-folding of an as-printed flat sheet into a more stable tubular shape at 80 °C, which can be regarded as the new permanent shape (the relaxation of residual stresses makes it more stable). The second step of shape memory, which involves thermo-mechanical programming of the hollow tube (*i.e.*, deformation of the hollow tube into a flat sheet at ≈ 40 °C and fixing it at ≈ 0 °C), results in shape recovery into hollow tubes at 37 °C. As a proof-of-concept study, HUVECs are used to demonstrate complete monolayer formation over the lumen, which could aid in improving the long-term patency of smaller-diameter vascular grafts. Overall, the dual shape morphing strategy enables the generation of complex shapes at much lower temperatures, which makes it promising for biofabrication. In future studies, multiple cell lines, such as vascular smooth muscle cells (VSMCs), can be incorporated to realize more mature and multifunctional vascular constructs. Combining FEA simulations, more complex and physiologically relevant designs, such as bifurcated vascular grafts, can be fabricated through this combinatorial fabrication approach. Apart from implantable customizable grafts, the sequential shape morphing feature can be utilized for realizing dynamic reconfigurable parts in applications such as sensors,⁶⁴ soft robotics,⁶⁵ *etc.*, by simple thermal stimulation.

Table 5 Comparison of dual shape morphing in this study with studies reporting either shape memory or programmable shape changes

Material used	Triggering stimulus and temperature (°C)	Shape memory property	Programmable shape change	Remarks	Ref.
PLMC	Direct heating, 45	Explored for 2D and 3D structures	No demonstration	<ul style="list-style-type: none"> Design and simulations for programmable and predictable shape change not explored 	16
PLMC/PTMC/Fe ₃ O ₄	Inductive heating, 45 and 80	Triple shape memory explored for selective shape recovery	No demonstration	<ul style="list-style-type: none"> Intrinsic triple shape memory of PLMC/PTMC blend and its composite with Fe₃O₄ demonstrated Lack of design-aided manufacturing and simulations to drive any shape change High triggering temperatures and bulky magnetic field setup limit achieving cellularized constructs 	60
ABS	Direct heating, 150	No demonstration, as ABS does not exhibit shape memory properties.	Demonstrated, but complete bending into hollow tubes not achieved	<ul style="list-style-type: none"> Comprehensive FEA simulations to predict shape changes for heterogeneous laminations lacking 	12
PLA	Direct heating, 85	No demonstration about retention of SM properties	Simulations performed to explore multimodal shape changes.	<ul style="list-style-type: none"> Shapes relevant for biomedical applications, such as hollow tubes were not achieved High activation temperatures, and the absence of dual shape morphing limit cellularization of the printed parts 	15
PLA	Direct heating, 85	No demonstration	Demonstrated, but no simulations	<ul style="list-style-type: none"> No predictive FEA simulations 	10
PLMC	Direct heating, 80	Demonstrated post-shape-change	Demonstrated, with quantitative FEA simulations	<ul style="list-style-type: none"> No relevant structures or proposed applications Programmable shape change with predictive FEA simulations Combination with shape memory to reduce triggering temperature Biofabrication with cellular constructs 	This work

5. Conclusion

This study utilizes a single medical-grade SMP to drive highly programmable and predictive shape deformation governed by infill angles and FEA simulations, respectively. The shape deformation is rapid (within one minute), complete (a fully sealed robust hollow tube forms from flat sheets), and occurs at much lower temperatures (≈ 80 °C). Close quantitative prediction was also established (< 0.2 mm error) between experimental observations and simulations that can help realize tubes with a range of diameters and lengths suiting a multitude of biomedical applications with great accuracy. Finally, as a proof of concept, vascular grafts with cellularized lumens were prepared by integrating shape morphing with the SM properties of PLMC. The tubes demonstrated good cell adhesion and complete cell coverage, which can improve the long-term patency of small-diameter vascular grafts. The dual and sequential shape morphing ability can open a plethora of opportunities in generating complex dynamic parts useful for a variety of fields, not limited to implants.

Conflicts of interest

The authors have filed for a patent application. There are no other competing interests to declare.

Acknowledgements

The authors acknowledge support from the Science and Engineering Research Board (SERB), Government of India (IPA/2020/000025). S. C. is supported by the Prime Minister's Research Fellowship.

References

- X. Kuang, D. J. Roach, J. Wu, C. M. Hamel, Z. Ding, T. Wang, M. L. Dunn and H. J. Qi, *Adv. Funct. Mater.*, 2019, **29**, 1805290.
- Y. S. Alsheby, M. Nafea, M. S. M. Ali and H. A. Almurib, *Eur. Polym. J.*, 2021, **159**, 110708.
- M. Rafiee, R. D. Farahani and D. Therriault, *Adv. Sci.*, 2020, **7**, 1902307.
- M. Behl, M. Y. Razzaq and A. Lendlein, *Adv. Mater.*, 2010, **22**, 3388–3410.
- L. Chen, H.-B. Zhao, Y.-P. Ni, T. Fu, W.-S. Wu, X.-L. Wang and Y.-Z. Wang, *J. Mater. Chem. A*, 2019, **7**, 17037–17045.
- J. Wang, X. Lin, R. Wang, Y. Lu and L. Zhang, *Adv. Funct. Mater.*, 2023, **33**, 2211579.
- H. Du, Y. Yu, G. Jiang, J. Zhang and J. Bao, *Macromol. Chem. Phys.*, 2011, **212**, 1460–1468.
- S. A. Pineda-Castillo, J. Luo, H. Lee, B. N. Bohnstedt, Y. Liu and C.-H. Lee, *Adv. Eng. Mater.*, 2021, **23**, 2100322.
- A. Bhargava, K. Peng, J. Stieg, R. Mirzaeifar and S. Shahab, *RSC Adv.*, 2017, **7**, 45452–45469.
- F. Wang, F. Luo, Y. Huang, X. Cao and C. Yuan, *Adv. Mater. Technol.*, 2023, **8**, 2201383.
- T. Y. Koh and A. Sutradhar, *Addit. Manuf.*, 2022, **56**, 102866.

- 12 B. Goo, C.-H. Hong and K. Park, *Mater. Des.*, 2020, **188**, 108485.
- 13 L. Ren, Z. Li, Q. Liu, L. Ren, Q. Wu, B. Li, G. Li, Z. Song and X. Zhou, *Adv. Mater. Technol.*, 2021, **6**, 2001289.
- 14 A. Joshi, S. Choudhury, V. S. Baghel, S. Ghosh, S. Gupta, D. Lahiri, G. K. Ananthasuresh and K. Chatterjee, *Adv. Healthcare Mater.*, 2023, 2300701.
- 15 B. Zou, C. Song, Z. He and J. Ju, *Extreme Mech. Lett.*, 2022, **54**, 101779.
- 16 X. Wan, H. Wei, F. Zhang, Y. Liu and J. Leng, *J. Appl. Polym. Sci.*, 2019, **136**, 48177.
- 17 S. Choudhury, A. Joshi, D. Dasgupta, A. Ghosh, S. Asthana and K. Chatterjee, *Mater. Adv.*, 2024, **5**, 3345–3356.
- 18 A. Joshi, S. Choudhury, S. Asthana, S. Homer-Vanniasinkam, U. Nambiar and K. Chatterjee, *Biomater. Sci.*, 2023, **11**, 7703–7708.
- 19 S. Choudhury, A. Joshi, D. Dasgupta, A. Ghosh, S. Asthana and K. Chatterjee, *Mater. Adv.*, 2024, **5**, 3345.
- 20 S. Basak and A. Bandyopadhyay, *Macromol. Chem. Phys.*, 2021, **222**, 2100195.
- 21 H. Xie, K.-K. Yang and Y.-Z. Wang, *Prog. Polym. Sci.*, 2019, **95**, 32–64.
- 22 X. Wan, L. Luo, Y. Liu and J. Leng, *Adv. Sci.*, 2020, **7**, 2001000.
- 23 X. L. Lu, W. Cai and Z. Y. Gao, *J. Appl. Polym. Sci.*, 2008, **108**, 1109–1115.
- 24 M. Bao, X. Lou, Q. Zhou, W. Dong, H. Yuan and Y. Zhang, *ACS Appl. Mater. Interfaces*, 2014, **6**, 2611–2621.
- 25 C. A. Gracia-Fernández, S. Gómez-Barreiro, J. López-Beceiro, J. Tarrío Saavedra, S. Naya and R. Artiaga, *Polym. Test.*, 2010, **29**, 1002–1006.
- 26 T. Sauter, M. Heuchel, K. Kratz and A. Lendlein, *Polym. Rev.*, 2013, **53**, 6–40.
- 27 N. Paunović, D. Meyer, A. Krivitsky, A. R. Studart, Y. Bao and J. C. Leroux, *J. Controlled Release*, 2023, **361**, 417–426.
- 28 J. Wang, H. Gao, Y. Hu, N. Zhang, W. Zhou, C. Wang, B. P. Binks and Z. Yang, *J. Mater. Sci.*, 2021, **56**, 731–745.
- 29 X. Wan, F. Zhang, Y. Liu and J. Leng, *Carbon*, 2019, **155**, 77–87.
- 30 M. N. Hassan, M. A. Yassin, A. M. Eltawila, A. E. Aladawi, S. Mohamed-Ahmed, S. Suliman, S. Kandil and K. Mustafa, *Biomater. Res.*, 2022, **26**, 55.
- 31 K. Mirasadi, D. Rahmatabadi, I. Ghasemi, M. Khodaei, M. Baniassadi and M. Baghani, *Macromol. Mater. Eng.*, 2024, 2400038.
- 32 T. T. Machairas, A. G. Solomou, A. A. Karakalas and D. A. Saravanos, *J. Intell. Mater. Syst. Struct.*, 2019, **30**, 2166–2185.
- 33 A. Kundu and A. Banerjee, *Thin Wall Struct.*, 2024, **195**, 111338.
- 34 P. Wriggers and T. A. Laursen, *Computational contact mechanics*, Springer, 2006.
- 35 A. Sydney Gladman, E. A. Matsumoto, R. G. Nuzzo, L. Mahadevan and J. A. Lewis, *Nat. Mater.*, 2016, **15**, 413–418.
- 36 Z. Jiang, B. Diggle, M. L. Tan, J. Viktorova, C. W. Bennett and L. A. Connal, *Adv. Sci.*, 2020, **7**, 2001379.
- 37 J. Liu, O. Erol, A. Pantula, W. Liu, Z. Jiang, K. Kobayashi, D. Chatterjee, N. Hibino, L. H. Romer and S. H. Kang, *ACS Appl. Mater. Interfaces*, 2019, **11**, 8492–8498.
- 38 M. Bodaghi, R. Noroozi, A. Zolfagharian, M. Fotouhi and S. Norouzi, *Materials*, 2019, **12**, 1353.
- 39 B. H. Walpoth and G. L. Bowlin, *Expert Rev. Med. Devices*, 2005, **2**, 647–651.
- 40 M. Trujillo-Miranda, I. Apsite, J. A. R. Agudo, G. Constante and L. Ionov, *Macromol. Biosci.*, 2023, **23**, 2200320.
- 41 Y. C. Shin, J. B. Lee, D. H. Kim, T. Kim, G. Alexander, Y. M. Shin, J. Y. Park, S. Baek, J. K. Yoon and Y. J. Lee, *Adv. Mater.*, 2019, **31**, 1904476.
- 42 W. Kitana, I. Apsite, J. Hazur, A. R. Boccaccini and L. Ionov, *Adv. Mater. Technol.*, 2023, **8**, 2200429.
- 43 J. Liu, O. Erol, A. Pantula, W. Liu, Z. Jiang, K. Kobayashi, D. Chatterjee, N. Hibino, L. H. Romer, S. H. Kang, T. D. Nguyen and D. H. Gracias, *ACS Appl. Mater. Interfaces*, 2019, **11**, 8492–8498.
- 44 S. B. Gugulothu and K. Chatterjee, *ACS Macro Lett.*, 2023, **12**, 494–502.
- 45 P. Mondal, A. Mandal and K. Chatterjee, *Adv. Mater. Technol.*, 2023, **8**, 2300894.
- 46 J. Shi, Y. Teng, D. Li, J. He, A. C. Midgley, X. Guo, X. Wang, X. Yang, S. Wang and Y. Feng, *Mater. Today Bio*, 2023, **21**, 100709.
- 47 A. Joshi, S. Choudhury, S. B. Gugulothu, S. S. Visweswariah and K. Chatterjee, *Biomacromolecules*, 2022, **23**, 2730–2751.
- 48 T. Van Manen, S. Janbaz and A. A. Zadpoor, *Mater. Horiz.*, 2017, **4**, 1064–1069.
- 49 K. Kapetanios, A. Light, N. Thakare, K. Mahbubani, K. Saeb-Parsy and K. Saeb-Parsy, *BJU Int.*, 2022, **130**, 408–419.
- 50 S. Choudhury, S. Asthana, S. Homer-Vanniasinkam and K. Chatterjee, *Biomater. Sci.*, 2022, **10**, 3716–3729.
- 51 S. L. M. Dahl, C. Rhim, Y. C. Song and L. E. Niklason, *Ann. Biomed. Eng.*, 2007, **35**, 348–355.
- 52 D. Camasão and D. Mantovani, *Mater. Today Bio*, 2021, **10**, 100106.
- 53 E. Sachyani Keneth, A. Kamyshny, M. Totaro, L. Beccai and S. Magdassi, *Adv. Mater.*, 2021, **33**, 2003387.
- 54 T. Gu, H. Bi, H. Sun, J. Tang, Z. Ren, X. Zhou and M. Xu, *Addit. Manuf.*, 2023, **70**, 103544.
- 55 G. Scalet, *Actuators*, 2020, **9**, 10.
- 56 F. Fazal, S. Raghav, A. Callanan, V. Koutsos and N. Radacsi, *Biofabrication*, 2021, **13**, 032003.
- 57 H. Rupp, D. Döhler, P. Hilgeroth, N. Mahmood, M. Beiner and W. H. Binder, *Macromol. Rapid Commun.*, 2019, **40**, 1900467.
- 58 J. F. Christ, N. Aliheidari, A. Ameli and P. Pötschke, *Mater. Des.*, 2017, **131**, 394–401.
- 59 X. Wan, H. Wei, F. Zhang, Y. Liu and J. Leng, *J. Appl. Polym. Sci.*, 2019, **136**, 48177.
- 60 X. Wan, Y. He, Y. Liu and J. Leng, *Addit. Manuf.*, 2022, **53**, 102689.
- 61 C. Lin, Z. Huang, Q. Wang, Z. Zou, W. Wang, L. Liu, Y. Liu and J. Leng, *Composites, Part B*, 2023, **256**, 110623.
- 62 M. Bustamante-Torres, D. Romero-Fierro, J. Estrella-Nuñez, B. Arcentales-Vera, E. Chichande-Proañón and E. Bucio, *Polymers*, 2022, **14**, 752.
- 63 G. Liu, J. Gao, H. Ai and X. Chen, *Small*, 2013, **9**, 1533–1545.
- 64 D. Chen, Q. Liu, Z. Han, J. Zhang, H. Song, K. Wang, Z. Song, S. Wen, Y. Zhou and C. Yan, *Adv. Sci.*, 2020, **7**, 2000584.
- 65 M. Y. Khalid, Z. U. Arif, W. Ahmed, R. Umer, A. Zolfagharian and M. Bodaghi, *Sens. Actuators, A*, 2022, **343**, 113670.